Available online at www.sciencedirect.com

ScienceDirect

Proceedings of the Combustion Institute 000 (2022) 1–10

Proceedings of the Combustion Institute

www.elsevier.com/locate/proci

Measurements of propane–O_2–Ar laminar flame speeds at temperatures exceeding 1000 K in a shock tube

Adam J. Susa*, Lingzhi Zheng, Ronald K. Hanson

Stanford University, Department of Mechanical Engineering, Stanford, CA, USA

Received 5 January 2022; accepted 22 July 2022
Available online xxx

Abstract

Laminar flame speed (S_L) measurements of stoichiometric propane in an oxygen-argon oxidizer were performed in a shock tube at unburned-gas temperatures of 296–1234 K and near-atmospheric pressures. Non-intrusive laser-induced breakdown is used to ignite expanding flames following the reflected-shock passage. Flame propagation is recorded using schlieren imaging in a recently implemented side-wall imaging flame test section (SWIFT). In a refined approach to account for flame distortion and the slight residual motion of the post-reflected-shock gas, an area-averaged formulation of the linear-curvature model (the AA-LC model) is derived for use extrapolating flame data to zero stretch. Measured S_L values extracted using the AA-LC model closely agree with previous experimental measurements performed in a conventional kinetics shock tube (CKST) using much smaller flame kernels. Below the chemistry-affected limit of 1050 K, experimental S_L values agree well with simulations performed using the detailed AramcoMech 3.0 kinetic mechanism; S_L values simulated with propane mechanisms from NUIG and San Diego are found to differ from the measurements by 10% or more. Over the wide temperature range of the present data, the ubiquitous power-law form of empirical fit is shown to be inadequate for capturing the S_L temperature dependence; a non-Arrhenius form is shown to perform favorably. The uncertainties of flame speed measurements performed in the SWIFT average 3.0% and 4.4% for experiments performed under static and post-reflected-shock conditions, respectively, a reduction from the 5.8% average uncertainty of CKST experiments. This work represents a significant step forward in the development of experimental capabilities for high-temperature flame speed measurements. The present results illustrate the potential value of the shock-tube flame speed method to provide measurements useful for informing kinetic model tuning and validation at conditions for which experimental data were not previously obtainable.

Keywords: Flame speed; Shock tube; Schlieren; Propane

* Corresponding author.
E-mail address: asusa@alumni.stanford.edu (A.J. Susa).

https://doi.org/10.1016/j.proci.2022.07.191
1540-7489

1. Introduction

At the extreme conditions reached within modern combustion engines, coupled ignition chemistry and flame propagation can jointly govern engine performance [1]. Zeldovich first considered the effect of unburned-gas reactivity on the flame propagation speed, determining that a continuum of solutions to the chemistry-affected deflagration speed are possible, bounded from below by the unaffected flame speed [2]. Numerous efforts to predict the behavior of laminar flames at reactive unburned-gas conditions have employed simulation-based methods [*e.g.*, [1,3–6], 7]. However, while experimental advancements have extended the range of unburned-gas pressure (P_u) accessible to laminar flame speed (S_L) measurements [*e.g.*, 8], practical limitations have made progress extending the accessible unburned-gas temperature (T_u) range more protracted.

To the authors' knowledge, the 873-K data reported by Kurata et al. using a Bunsen-flame configuration [9] represent the S_L measurements at the highest T_u reported in the literature prior to the introduction of the shock-tube flame speed method. The confined spherically expanding flame (CSEF) method has been demonstrated up to 720 K [10]. Heated, diverging channels have been employed in S_L measurements up to about 650 K [*e.g.*, 11]. Rapid compression machines (RCMs) have been employed to measure burning velocities at T_u up to about 1000 K, but flame wrinkling and pressure rise typically precludes the determination of S_L values [12].

The introduction of the shock-tube flame speed method by Ferris et al. promised to enable experimental study at never-before-accessible, high-T_u conditions, beginning with their initial demonstration of propane/air flame speed measurements at T_u up to 832 K [13]. In early shock-tube flame speed studies, the onset of instabilities limited the highest T_u at which S_L could be measured. This limitation was finally overcome through the use of argon (Ar) dilution and ignition nearer to the end wall in [14], measurements which serve as a point of comparison to the present work. Early applications of side-wall imaging to flame experiments additionally provided insights into the dynamics of flames generated in a shock-tube environment [15–17].

In the present study, a combination of experimental and analytical enhancements to the shock-tube flame speed method are applied in propane S_L measurements at temperatures in excess of 1000 K. Large-field-of-view (-FOV) side-wall schlieren imaging is applied in a novel, side-wall imaging flame test section (SWIFT) featuring large side-wall windows [18, Ch. 6]. In this work, a refined analysis method is derived and applied to extract the area-averaged burning velocities ($\bar{S}_b$) and curvatures ($\bar{\kappa}$) from rotationally symmetric flames typical in the shock tube, which are used to determine unstretched, unburned flame speeds (S_u^0) at T_u conditions reaching the limit of spontaneous unburned-gas reactivity.

2. Theoretical development

Within a spherically expanding flame (SEF) ignited in quiescent unburned gas, the burned gas remains stationary. For this reason, the displacement speed observed as the time derivative of the flame radius ($\dot{r}_f$) can be taken as the burned flame speed (S_b), the flame speed relative to the burned gas [19]. Unlike the unstretched, planar flames for which S_L is defined, conditions which cannot be experimentally realized, SEFs are subject to positive flame stretch (K) that causes $S_b(K)$ to differ from the unstretched, burned flame speed (S_b^0). In order to estimate S_b^0, S_b measurements recorded over a range of K conditions are commonly projected to zero stretch using physics-based extrapolations.

The choice of extrapolation function is the topic of ongoing debate. A discussion of the selection of the linear-curvature (LC) model in this work follows; a more complete review of the literature can be found in [18, pp. 32–40]. Markstein [20] first proposed the LC model:

$$S_b = S_b^0(1 - L_b\kappa), \tag{1}$$

where κ is the total curvature of the surface ($\kappa = 2/r_f$ for a spherical flame) and L_b is the Markstein length. The linear-stretch (LS) model:

$$S_b = S_b^0 - L_bK, \tag{2}$$

was proposed somewhat later [*e.g.*, 21] but gained dominance in the interpretation of experimental measurements. For a spherical flame, $K = S_b(2/r_f)$.

More recently, the need to account for nonlinear stretch effects became apparent [22], and numerous extrapolation models (including LC) have been considered for their ability to capture nonlinear stretch effects. The nonlinearity of the LC model is seen by recasting the spherical form of Eq. (1) in terms of K, giving:

$$S_b = S_b^0 - \left(S_b^0/S_b\right)L_bK. \tag{3}$$

Here, it is apparent that the LC model is nonlinear in terms of K as a result of the additional (S_b^0/S_b) term compared to the LS model. Analyses by Chen [23] and Cai et al. [24] both conclude that the LC model provides more accurate results than the more commonly used expression proposed by Kelley and Law [22] when the Lewis number is greater than unity ($L_b > 0$). For this reason, the LC model (Eq. (1)) is utilized in the present study.

In practice, a perfectly spherical flame is rarely realized. Within static vessels ignited using electric sparks, the interaction of the flame with the electrodes locally perturbs the flame surface. For low-speed flames, buoyant effects can lead to mild flame

Please cite this article as: A.J. Susa, L. Zheng and R.K. Hanson, Measurements of propane–O<ce:inf>2</ce:inf>–Ar laminar flame speeds at temperatures exceeding 1000 K in a shock tube, Proceedings of the Combustion Institute, https://doi.org/10.1016/j.proci.2022.07.191

distortion [e.g., 25]. When laser-induced plasma ignition (LIPI) is used to ignite a flame, the toroidal flow field produces an aspherical flame kernel [e.g., 13]. Recently, expanding flames in a shock tube were found through side-wall imaging to exhibit sometimes-significant axial distortion [15,17].

Distorted flames often exhibit locally smooth surfaces, such that correct handling of their structure may allow them to be used as a basis for S_L measurements. Considering an expanding flame of total flame-front area A_f, the total mass burning rate ($\dot{M}_f$) is defined as the surface integral of the local burning flux, $\dot{m}_f = \rho_b S_b$, where ρ_b is the burned-gas density:

$$\dot{M}_f = \int_{A_f} \dot{m}_f dA = \rho_b \int_{A_f} S_b dA. \quad (4)$$

Substitution of the LC model (Eq. (1)) provides a functional form of S_b in the expression:

$$\dot{M}_f = \rho_b \int_{A_f} S_b^0 (1 - L_b \kappa) dA \quad (5)$$

where L_b is constant for a given unburned-gas state and κ is the local, total curvature of the flame front.

From the simple expression for the mass of burned gas, $M_b = V_b \rho_b$, where V_b is the burned-gas volume, the rates $\dot{M}_b$ and $\dot{V}_b$ can likewise be related:

$$\dot{M}_b = \dot{V}_b \rho_b. \quad (6)$$

Recognizing $\dot{M}_b = \dot{M}_f$ by continuity, Eqs. (5) and (6) can be equated and simplified:

$$\frac{\dot{V}_b}{A_f} = S_b^0 \left(1 - \frac{L_b}{A_f} \int_{A_f} \kappa dA\right). \quad (7)$$

Defining the area-averaged burning speed, $\bar{S}_b$, and total curvature, $\bar{\kappa}$:

$$\bar{S}_b \equiv \dot{V}_b / A_f \quad (8)$$

$$\bar{\kappa} \equiv \frac{1}{A_f} \int_{A_f} \kappa dA, \quad (9)$$

Equation (7) can be converted to a form equivalent to the original LC model (Eq. (1)):

$$\bar{S}_b = S_b^0 (1 - L_b \bar{\kappa}) \quad (10)$$

The basis of Eq. (10) on area-averaged properties is significant in that it allows for exact accounting of local propagation characteristics, unlike the approximate form of a previous aspheric correction [13]. The relevant parameters V_b, A_f, and $\bar{\kappa}$ are inherently insensitive to bulk motion of the flame, an advantageous property when applied to shock-tube experiments where small residual velocities do exist [16].

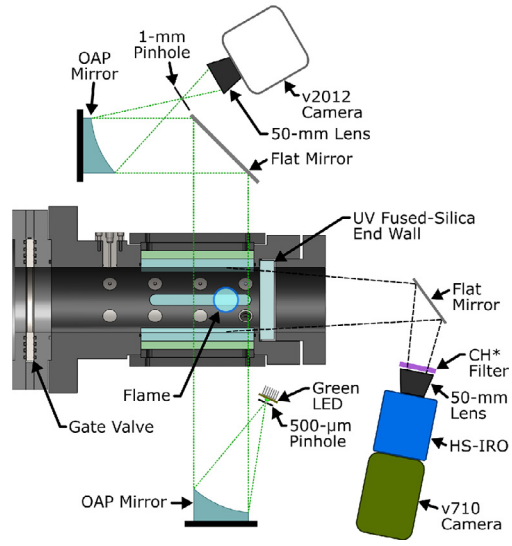

Fig. 1. SWIFT experimental configuration shown as a top-down cross-sectional view. Curved side-wall windows provide a 18- x 6.4-cm lateral field of view. The ignition laser (not shown) is orthogonal to the view. Cross sections to scale; imaging instrumentation and ray tracing approximate.

3. Methodology

3.1. Experimental setup

The shock tube used throughout this work features a 11.53-cm inner diameter, 9.76-m-long driven section, and variable length driver section. Previous shock-tube flame studies [*e.g.*, 13,14] were performed in the conventional kinetics shock tube (CKST) configuration, as described by Campbell et al. [26], which afforded very limited side-wall optical access. The new SWIFT, shown schematically in Fig. 1, replaces the old test section (between the gate vale and driven end wall) with a new, anodized-aluminum, optically accessible test section.

Stoichiometric ($\phi = 1$) unburned-gas mixtures of propane (C_3H_8) in an oxidizer comprised of 21% oxygen (O_2) and 79% argon (Ar) are prepared manometrically in a stainless-steel mixing tank. Following at least one hour of mixing by a mechanical vane, the premixed test-gas is introduced into the evacuated shock-tube driven section to an initial (region-1) pressure, P_1, and ambient temperature, T_1. The driver section, initially separated from the driven section by a polycarbonate diaphragm, is then filled with helium and nitrogen until the diaphragm ruptures.

The sudden diaphragm rupture produces a shock wave in the test gas, accelerating it and elevating T and P to post-incident-shock (region-2) conditions. Upon reaching the driven-section end wall, the shock wave reflects, further elevating T

Please cite this article as: A.J. Susa, L. Zheng and R.K. Hanson, Measurements of propane–O<ce:inf>2</ce:inf>–Ar laminar flame speeds at temperatures exceeding 1000 K in a shock tube, Proceedings of the Combustion Institute, https://doi.org/10.1016/j.proci.2022.07.191

and P as the gas is stagnated at the post-reflected-shock (region-5) conditions. The incident shock speed is measured by a series of pressure transducers positioned along the driven section. The region-5 state, which defines the unburned-gas conditions for flame experiments, are calculated using the chemically frozen shock solver FROSH with the end-wall extrapolated shock speed and assuming vibrational equilibrium in regions 2 and 5 [27]. The uncertainty of the region-5 conditions is calculated at the 95% confidence level based contributions from the initial conditions and measured shock speed. The fuel mole fraction is measured *in situ* using a 3.41 μm laser absorbance diagnostic [28].

Expanding flames are ignited behind the reflected shock by LIPI [13]. A Q-switched, frequency-doubled Nd:YAG laser (Solo PIV 120, 532 nm) serves as the laser source. A $f = 15$ cm lens focuses the beam to a waist of $\mathcal{O}(10\ \mu\text{m})$ diameter where laser-induced breakdown occurs, igniting a flame. Spark delays following the reflected shock were less than 0.5 ms for experiments with $T_u > 1000$ K and less that 1 ms for those performed at lower T_u. Laser-energy control is achieved with a variable attenuator. Spark energies in SWIFT experiments were estimated using differential energy measurements to be 1–2 mJ;

Schlieren imaging is performed through the side walls of the shock tube. In the previous work utilizing the CKST [14], the small ports restricted the schlieren FOV to a diameter of about 1.5 cm. In the SWIFT, large side-wall windows designed as afocal cemented-doublet cylindrical lenses provide optical access for large-FOV schlieren imaging [18, Ch. 6] and allow flames to be observed to much larger r_f. A high-power light-emitting diode (LED) paired with a pinhole serves as the schlieren light source; while a white LED was used with the CKST, a green LED is used in the SWIFT to minimize chromatic aberrations. Both the CKST and SWIFT experiments utilize symmetric schlieren stops (slit and pinhole, respectively) to produce isotopic responses to density gradients [29], which is preferable for the consistent detection of a circular flame front. A detailed comparison of the schlieren systems used with the CKST [14] and SWIFT (this work) can be found in Supplement 1, Table S1. Further discussion of the use of off-axis parabolic (OAP) mirrors in the SWIFT schlieren arrangement can be found in [30].

3.2. Image processing

Flame front positions are extracted from each schlieren video frame using active-contouring [31], implemented in Scikit-Image [32]. Prior to contouring, images are first background normalized to homogenize non-uniformity in the illumination intensity. Next, sequential images are differenced, and positive values in the resulting images are truncated, to eliminate slow-varying background artifacts while enhancing the fast-moving flame front. Finally, a Gaussian blurred copy of the difference image is superimposed onto the difference image to provide a spatially distributed gradient for the contour to follow.

Active contouring is applied sequentially to each frame of the video sequence in reverse order, with the optimal contour of each frame serving as the initial guess for the previous frame of the sequence. After each contour is optimized, the X–Y coordinates are parameterized and interpolated to a fixed spacing to prevent the clustering of the points through successive optimization steps. Sample optimized contours overlaid on processed schlieren images are provided in Supplement 1, Fig. S1. Example images at all processing steps can be found in [18, pp. 121–128].

3.3. Flame speed extraction

Prior works have shown flames ignited in a shock tube tend to exhibit substantial radial symmetry about the axis of the tube even in the presence of significant axial distortion [15,17]. This behavior was confirmed for flames studied in the present investigation through a qualitative assessment of end-wall emission images, in which flames appear generally circular regardless of the presence of axial distortion as seen in the side-wall view. As such, an approximation of cylindrical symmetry is adopted for representing the morphology in order to perform the property integrals. Defining the horizontal direction, z, as the axis of symmetry, the flame radius, $r_f(z)$, is approximated as:

$$r_f(z) = \delta(z)/2, \tag{11}$$

where $\delta(z)$ is the total vertical extent of the optimal contour (Supplement 1, Fig. S2a).

Values of V_b, A_f, and $\bar{\kappa}$ are evaluated as follow:

$$V_b = \pi \int_0^{z_f} r_f^2 \mathrm{d}z \tag{12}$$

$$A_f = 2\pi \int_0^{z_f} r_f \sqrt{1 + r_f'^2}\,\mathrm{d}z \tag{13}$$

$$\bar{\kappa} = \frac{1}{A_f} \int_0^{z_f} \kappa(z) r_f \sqrt{1 + r_f'^2}\,\mathrm{d}z, \tag{14}$$

with numerical integration performed using Simpson's method as implemented in Scipy [33]. The local, total curvature (κ) in Eq. (14) is taken as:

$$\kappa(z) = \frac{-r_f''}{\left(1 + r_f'^2\right)^{3/2}} + \frac{1}{r_f\left(1 + r_f'^2\right)^{1/2}} \tag{15}$$

where r_f' and r_f'' are the first and second derivatives of r_f with respect to z, respectively. Equation (15) is

Please cite this article as: A.J. Susa, L. Zheng and R.K. Hanson, Measurements of propane–O<ce:inf>2</ce:inf>–Ar laminar flame speeds at temperatures exceeding 1000 K in a shock tube, Proceedings of the Combustion Institute, https://doi.org/10.1016/j.proci.2022.07.191

adapted from Spivak [34] and confirmed to recover the expected result of $\kappa = 2/r_f$ for a sphere.

Time-series data for properties $\chi \in \{\bar{\kappa}, A_f, V_b\}$ are converted to effective radii, $\mathcal{R}_\chi$:

$$\mathcal{R}_\kappa = 2/\kappa \tag{16}$$

$$\mathcal{R}_A = (A_f/4\pi)^{1/2} \tag{17}$$

$$\mathcal{R}_V = (3V_b/4\pi)^{1/3} \tag{18}$$

before being smoothed with a second-order Savitzky-Golay filter [33,35]. The conversions of Eqs. (16)–(18) are then reversed, converting the smoothed $\mathcal{R}_\chi$ to smoothed time-series data, χ. $\dot{V}_b$ values (used in Eq. (8)) are calculated from smoothed V_b data using a third-order, first-derivative Savitzky-Golay filter.

A linear fit of the form of Eq. (10) applied to the smoothed $\bar{S}_b$ and $\bar{\kappa}$ is used to extract S_b^0 and L_b. The subset of data over the $\bar{\kappa}$ range 1.15–4 cm^{-1} are typically used in performing the fit, corresponding to an equivalent r_f range 0.5–1.75 cm. The 1.75-cm upper radius limit is selected as 30% that of the shock-tube based on the cylindrical confinement criteria of Burke et al. [36]. The 0.5-cm lower limit is selected to avoid fitting data showing evidence of ignition effects or for which the active contour solution becomes unstable. The linear fit is found to be inherently insensitive to residual waviness in the $\bar{S}_b$ data, which tends to be present at periods longer than the filter window.

Extrapolated values S_b^0 are converted to the unburned-gas reference frame using the density ratio:

$$S_u^0 = (\rho_b/\rho_u)S_b^0. \tag{19}$$

Region-5 conditions provide the unburned-gas density (ρ_u); ρ_b is estimated from constant-P thermo-chemical equilibrium, evaluated with Cantera [37].

4. Results and discussion

In this section, the results of propane–O_2–Ar ($\phi = 1$) flame-speed experiments are presented and discussed. The present discussion focuses primarily on the experimental determination of S_L; values of L_b are presented for completeness but not discussed in depth. Static flame experiments exhibiting nearly spherical flames are first evaluated to assess the AA-LC model under ideal conditions. Flames ignited behind reflected shocks ($T_u \sim 650$ K) and exhibiting differing degrees of distortion are next evaluated to assess the performance of the AA-LC model when distortion is present. Finally, measurements obtained from new experiments performed at higher T_u are reported along with a detailed treatment of uncertainty.

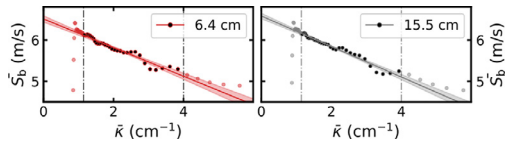

Fig. 2. Sample $\bar{S}_b$–$\bar{\kappa}$ extrapolations for two static flame experiments (T_u= 296 K, P_u= 1 atm). The gray, vertical lines represent the limits of data used in the AA-LC fit.

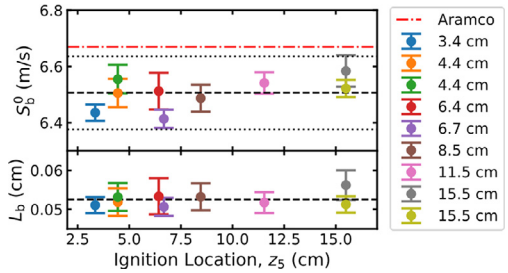

Fig. 3. S_b^0 (top) and L_b (bottom) measurements extracted from static-flame experiments using the AA-LC model. The black dashed line represents the mean of the measured values; the dotted lines mark ±2%. The red dot-dashed line shows the value S_b^0 calculated with AramcoMech 3.0 [38]. (For interpretation of the references to color in this figure legend, the reader is referred to the web version of this article.)

4.1. Static, spherical-flame validation

In order to evaluate the performance and repeatability of the AA-LC model as presently implemented, it is first applied in the analysis of static experiments ($T_u = 296 \pm 1$ K) exhibiting nearly spherical flames borrowed from a prior study [17]. Figure 2 shows example AA-LC extrapolations of $\bar{S}_b$–$\bar{\kappa}$ data obtained from two of the nine static experiments analyzed (all fits can be seen in Supplement 1, Fig. S2). The legends indicate the ignition locations, measured from the end wall. Lines mark best fits and shaded region represent the 95% confidence intervals.

Values of S_b^0 and L_b obtained from the static experiments are shown in Fig. 3. Error bars in Fig. 3 represent only the uncertainty of the linear fits evaluated at the 95% level. Black dashed lines mark the mean values. The mean uncertainty of the S_b^0 fits is 0.7% across static experiments. The standard deviation of the S_b^0 values is 0.8%, from which the 95% confidence interval of the random error is calculated to be 1.8% using Student-t statistics [39]. The combined uncertainty of the fit and random error is found to be 2%, marked by black dotted lines in Fig. 3 which nearly encompass the value S_b^0 simulated by AramcoMech 3.0 [38] (red dashed line).

Please cite this article as: A.J. Susa, L. Zheng and R.K. Hanson, Measurements of propane–O<ce:inf>2</ce:inf>–Ar laminar flame speeds at temperatures exceeding 1000 K in a shock tube, Proceedings of the Combustion Institute, https://doi.org/10.1016/j.proci.2022.07.191

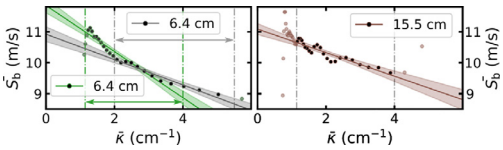

Fig. 4. $\bar{S}_b$–$\bar{\kappa}$ extrapolations for post-shock validation experiments. Plot legends indicate the ignition location. Two fits are shown for the 6.4-cm flame (left); the green fit covers the same $\bar{\kappa}$ range as other experiments, while the gray line is fit over a range 2–5.5 cm^{-1}. (For interpretation of the references to colour in this figure legend, the reader is referred to the web version of this article.)

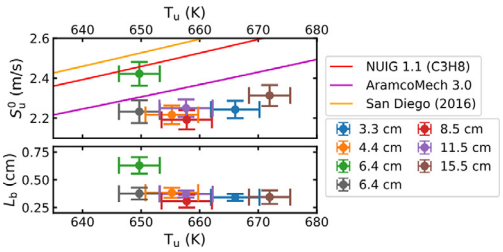

Fig. 5. S_u^0 (top) and L_b (bottom) measurements from post-shock validation experiments. Simulated S_L values are shown for comparison. (For interpretation of the references to colour in this figure legend, the reader is referred to the web version of this article.)

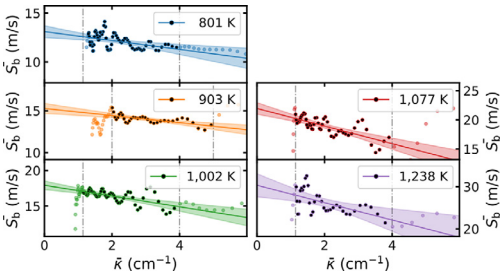

Fig. 6. $\bar{S}_b$–$\bar{\kappa}$ extrapolations for high-T_u experiments. T_u (*i.e.*, T_5) is labeled in the legends.

4.2. Post-shock, distorted-flame validation

A primary motivation of the AA-LC model is to enable the use of distorted flames in reliable S_u^0 measurements. This ability is evaluated using six flames ignited in a post-reflected-shock environment at $T_u \sim 650$ K and exhibiting differing degrees of distortion [17]. $\bar{S}_b$–$\bar{\kappa}$ data and AA-LC extrapolations for two experiments are shown in Fig. 4; plots for all experiments can be found in Supplement 1, Fig. S3. Values of S_u^0 and L_b are shown in Fig. 5, along with curves of simulated values using AramcoMech 3.0 [38] and propane-specific skeletal mechanisms from NUIG 1.1 [40] and San Diego [41]. In Fig. 5, vertical error bars contain contributions from the fit uncertainty and random error (taken as 1.8% from static experiments); horizontal error bars show the T_5 uncertainty.

The 6.4-cm ignition location (Fig. 4, left) represents the single worst-case of flame distortion. For the 6.4-cm flame, two fits are performed: one over the typical range $\bar{\kappa}$ and a second over the range 2–5.5 cm^{-1}. Using the standard $\bar{\kappa}$ range (green), the value S_u^0 exceeds that obtained from the other experiments by about 10%; the corresponding value L_b is over twice that of the other experiments. When higher-$\bar{\kappa}$ data is instead fit (*i.e.*, smaller r_f when the flame is less distorted; shown as gray), the values obtained for both S_u^0 and L_b are found to closely agree with those of the other experiments. As such, the ability of the AA-LC model to correctly account for all but the most severe distortion is confirmed. Consistency of extracted L_b values is additionally found to be a useful check that appropriate ranges of data are used in performing AA-LC extrapolations.

4.3. High-temperature results

Having validated the AA-LC model, S_u^0 measurements are reported and discussed for propane–O_2–Ar experiments ($\phi = 1$) at highest-ever-T_u conditions. Five experiments were performed in the SWIFT over the range 801 K $\leq T_u \leq$ 1238 K. In the 1238-K experiment, fuel loss was observable in the 3.41-μm measurement beginning immediately after passage of the reflected shock, confirming the spontaneously reactive nature of the unburned at the highest T_u.

Combined with the validation experiments of the previous sections, S_u^0 and L_b measurements are reported over the unprecedented range 296–1238 K (Fig. 7). Across the post-reflected-shock SWIFT experiments, the mean P_u was 1.03 atm, with a standard deviation of 0.03 atm. The mean, measured ϕ was 1.02 with a standard deviation of 0.01. Vertical error bars for L_b values are shown based on the 95% confidence interval of the fit parameters. Error bars for S_u^0 values are not shown in Fig. 7a, as they would be too small to see clearly, but are presented following a discussion of S_u^0 uncertainty in Fig. 8. Details of each SWIFT experiment are tabulated in Supplement 1, Table S2. Shown for comparison are results from earlier shock-tube flame speed measurements performed in the CKST [14].[1] While the values L_b extracted from CKST experiments using radius-based S_b and κ data obtained

[1] T_5 values reported for CKST experiments were recalculated in this work using the correct equilibrium-equilibrium FROSH constraint [27] and are thus higher by 30–50 K than T_5 values reported in [14], which were calculated using the incorrect frozen-equilibrium assumption.

Please cite this article as: A.J. Susa, L. Zheng and R.K. Hanson, Measurements of propane–O<ce:inf>2</ce:inf>–Ar laminar flame speeds at temperatures exceeding 1000 K in a shock tube, Proceedings of the Combustion Institute, https://doi.org/10.1016/j.proci.2022.07.191

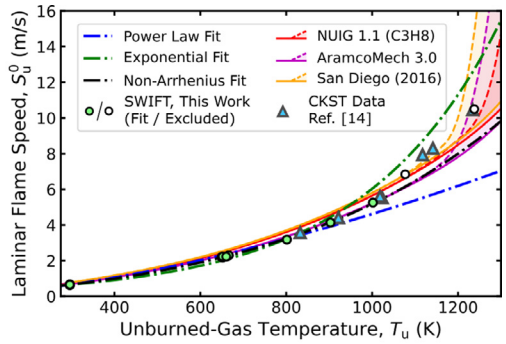

(a) S_u^0 Results

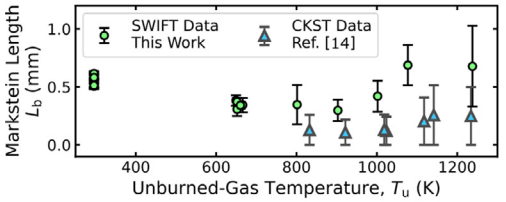

(b) L_b Results

Fig. 7. Flame speed and Markstein length results obtained from shock-tube flame speed experiments. Experimental data are shown as markers. Lines show flame speeds simulated using two different domain lengths: 1-cm (solid) and 6-cm (dashed). Dot-dashed lines represent empirical fits to the $T_u < 1050$ K SWIFT data (green-filled circles). (For interpretation of the references to colour in this figure legend, the reader is referred to the web version of this article.)

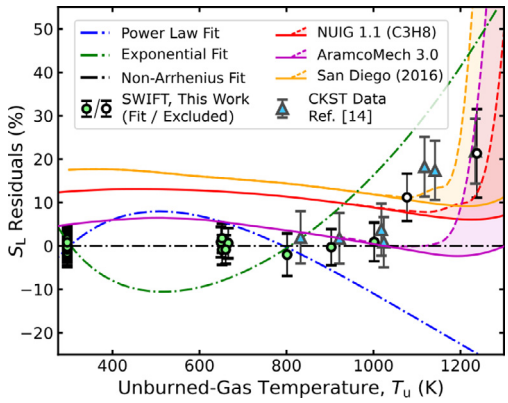

Fig. 8. S_L residuals of measurements, simulations, and fits all computed relative to the non-Arrhenius empirical fit. (For interpretation of the references to colour in this figure legend, the reader is referred to the web version of this article.)

from very small flame kernels (2–7 mm) are found to be systematically smaller than those obtained from SWIFT experiments, the values S_u^0 obtained from the two sets of experiments are found to agree quite closely.

S_L values simulated using the AramcoMech 3.0 detailed mechanism [38] and skeletal propane mechanisms from NUIG 1.1 [40] and San Diego [41] are shown in comparison to measured S_u^0 data. In order to provide a first-order accounting of chemistry effects on the flame speed at reactive values T_u, simulations were performed using two different calculation domain lengths (ℓ_{sim}) in the Chemkin-Pro PREMIX solver, a method previously reported in the literature [e.g. 3, 4]. With the flame centered in the simulation domain, the induction time (τ_{in}) between when the unburned gas enters the simulation domain and when it reaches the flame is $\tau_{in} \approx (\ell_{sim}/2)/S_L$. Considering high-$T_u$ conditions with $S_L \sim \mathcal{O}(10$ m/s), the chosen domain lengths of 1 cm (solid lines) and 6 cm (dashed lines) represent $\tau_{in} \sim 0.5$ and 3 ms, time scales representative of time of the spark after the reflected shock on the low end and an upper bound on the total measurement time on the high end.

The difference between the values S_L simulated with different ℓ_{sim} (shaded regions) bound a continuum of flame speeds that may be encountered as a result of chemistry effects on the relevant time scale [2]. At temperatures below $T_u \sim 1050$ K, both values ℓ_{sim} return effectively the same simulated value S_L for all mechanisms, indicating the unburned gas is chemically frozen over the experimental timescale of τ_{in} at these temperatures. However, values S_L simulated with different ℓ_{sim} diverge at higher T_u, demonstrating that chemistry effects become relevant beyond that T_u. For this reason, only that data for which $T_u < 1050$ K (green-filled circles) are considered in the empirical fits discussed next. Chemistry-affected data at higher T_u (white-filled circles) are included in the plots to illustrate the manifestation of chemistry effects in measurements.

The dot-dashed lines in Fig. 7a show empirical fits of the SWIFT S_u^0 measurements ($T_u < 1050$ K) following three functional forms. The empirically determined power-law model (blue line):

$$S_L = S_{L,0}(T_u/T_0)^{\alpha}, \tag{20}$$

is ubiquitous in the literature, with considerable effort having been made to quantify and report values of the temperature exponents (α) [42]. Two other functional forms are also evaluated, an exponential form:

$$S_L = S_{L,0} \exp\left(\frac{T_u - T_0}{T_{exp}}\right), \tag{21}$$

and a non-Arrhenius form that combines the exponential and power-law forms:

$$S_L = S_{L,0}\left(\frac{T_u}{T_0}\right)^{\alpha} \exp\left(\frac{T_u - T_0}{T_{exp}}\right). \tag{22}$$

In the latter two forms, T_{exp} is a characteristic temperature. Parameters of all three empirical fits are

Please cite this article as: A.J. Susa, L. Zheng and R.K. Hanson, Measurements of propane–O<ce:inf>2</ce:inf>–Ar laminar flame speeds at temperatures exceeding 1000 K in a shock tube, Proceedings of the Combustion Institute, https://doi.org/10.1016/j.proci.2022.07.191

Table 1
Empirical Fitting Parameters.

Empirical Form	Eqs.	$S_{L,0}$ (cm/s)	α (–)	T_{exp} (K)
Power Law	(20)	66.5	1.61	–
Exponential	(21)	66.9	–	318
Non-Arrhenius	(22)	66.5	0.95	767

tabulated in Table 1; an evaluation of empirical forms' performances is provided in the discussion of Fig. 8.

4.4. Measurement uncertainty

Sources and magnitudes of uncertainty are next considered for the S_u^0 measurements. In the discussion that follows, all sources of uncertainty are quantified at the 95% confidence level using small-population (Student-t) statistics [39] where appropriate. Already discussed in the static validation section, each S_u^0 measurement has an uncertainty associated with the linear fit to the $\bar{S}_b$–$\bar{\kappa}$ data; in this work, the mean fit uncertainty is found to be 0.7% across static experiments and 2.6% in post-reflected-shock experiments. The random measurement error was estimated from the static validation experiments to be 1.8%; this value is assumed to apply across all S_u^0 measurements reported here. The choice of the functional form used to extrapolate data (LC in this work) has itself been argued to be a source of uncertainty. Using the correlation reported by Huo et al. [43], the uncertainty of SWIFT experiments attributed to the extrapolation method (for which the $R_{f,new}$ evaluates to 0.67 cm) is found to be 2.3%. By comparison, CKST experiments have a 5.4% extrapolation-method uncertainty due to the use of smaller flames ($R_{f,new} = 0.24$ cm).

Uncertainty in the experimental conditions (T_5 and P_5) also contribute to the overall measurement uncertainty and are evaluated for the SWIFT experiments. For shocked experiments, uncertainties of T_5 and P_5 include contributions from the incident-shock velocity (V_{is}, evaluated as the 95% confidence interval of extrapolated end-wall value) as well at the initial conditions — T_1, P_1, and the test-gas composition (x_i) — for which uncertainties are estimated as 0.5 K, 0.5%, and 0.5%, respectively. The contributions of V_{is}, T_1, P_1, and x_i on T_5 and P_5 are propagated using numerical derivatives and combined as a root-sum-square of the components, providing mean T_5 and P_5 uncertainties of 0.6% and 1.5%, respectively, in post-reflected-shock experiments.

Contributions to S_u^0 uncertainty from the experimental conditions are propagated using derivative of the empirical non-Arrhenius fit for T_5 and a power-law fit for P_5 (taking $\beta \approx 0.35$ from Konnov et al. [42]), leading to the finding that uncertainty of T_5 contributes an average 1.3% uncertainty to S_u^0, while P_5 contributes only 0.5% in shocked experiments. In static experiments, T_u contributes 0.5% and P_u contributes 0.2%. In general, uncertainty in ϕ would also contribute to the S_u^0 uncertainty; however, at $\phi \approx 1$, $dS_u^0/d\phi \approx 0$ such that the contributions of the average 0.7% ϕ uncertainty and the 2% deviation of the mean measured ϕ from the nominal value of unity are negligible.

An alternative view of the S_u^0 results is provided in Fig. 8, where residuals calculated against the non-Arrhenius empirical fit are presented for all values shown in Fig. 7a. Vertical error bars represent the total uncertainty related to both the extrapolation and experimental conditions for SWIFT results; those for CKST results include only uncertainties associated with the extrapolation (fit, model, random error). Horizontal error bars are not shown, as vertical error bars include uncertainty from T_u. The mean uncertainty is found to be 3.0% for static experiments in the SWIFT and 4.4% for SWIFT experiments performed behing reflected shocks. The mean uncertainty of CKST experiments is larger, at 5.8%. Uncertainty related to image processing and the calculation of area-averaged properties is not treated in the present analysis but should be considered as a topic for future study.

The non-Arrhenius fit is seen to capture the temperature trends of both the data and the simulations well; the common power-law fit and alternative exponential fit both systematically fail to capture the trend of S_u^0 over the wide T_u range studied in this work. S_L values simulated with AramcoMech 3.0 are found to agree very well with the measurements up to 1000 K; at higher T_u, the measurements diverge from the 1-cm-ℓ_{sim} simulation results, the expected result of chemistry effects. Discrepancies on the order of 10–20% between the measurements and values S_L simulated using the other two mechanisms illustrate the opportunity for mechanism refinement using experimental S_u^0 measurements.

5. Conclusions

Flame speed measurements at extreme temperatures in excess of 1000 K are reported using the shock-tube flame speed method. Schlieren images were used to track the boundary of the flame through time. Area-averaged flame properties were then extracted using a novel analysis methodology (the AA-LC model) to accurately account for the details of aspherical flames. A detailed evaluation found the average S_u^0 uncertainty to be 4.4% in post-reflected-shock measurements performed in the SWIFT; uncertainty was higher (5.8%) for S_u^0 measurements based on smaller flames in the CKST configuration. Measured S_u^0 closely agreed with S_L values simulated using AramcoMech 3.0; propane-specific mechanisms from both NUIG 1.1 and San Diego were found to systematically over predict

Please cite this article as: A.J. Susa, L. Zheng and R.K. Hanson, Measurements of propane–O<ce:inf>2</ce:inf>–Ar laminar flame speeds at temperatures exceeding 1000 K in a shock tube, Proceedings of the Combustion Institute, https://doi.org/10.1016/j.proci.2022.07.191

the measured values. Discrepancies between some mechanisms and measurements illustrate the potential value of the shock-tube flame speed method to enable kinetic investigations at previously inaccessible and completely unvalidated conditions. Measurements were also evaluated against three forms of empirical fits, revealing that the common power-law fit fails to capture the T_u dependence over wide ranges but that an alternative non-Arrhenius form performs much better in capturing the T_u trend of the new measurements.

The present work provides a step towards enabling several significant opportunities for future study, of which two are highlighted. First, at reactive conditions ($T_u > 1050$ K), it should be possible to use laser diagnostics or other methods to characterize the evolution of the unburned-gas state, potentially providing a basis for performing reliable chemistry-affected S_u^0 measurements (something first attempted in [44]). The AA-LC model also provides an opportunity for improved interpretation of wall-bounded flames, potentially supporting their use as a basis of reliable S_u^0 measurements in both rapid-compression machines [45] or in the shock tube [17].

Declaration of Competing Interest

The authors declare that they have no known competing financial interests or personal relationships that could have appeared to influence the work reported in this paper.

Acknowledgments

This work was supported by the U.S. National Science Foundation under award number 1940865, contract monitor Dr. John Daily. Instrumentation used in this work was funded by the U.S. Army Research Office under award number W911NF-20-1-006, contract monitor Dr. Ralph Anthenien.

Supplementary material

Supplementary material associated with this article can be found, in the online version, at 10.1016/j.proci.2022.07.191.

References

[1] K.V. Puduppakkam, A.U. Modak, C. Wang, D. Hodgson, C.V. Naik, E. Meeks, Generating laminar flame speed libraries for autoignition conditions, Turbo Expo: Power for Land, Sea, and Air, vol. 84133, ASME, 2020. V04BT04A004
[2] Y. Zeldovich, Flame propagation in a substance reacting at initial temperature, Combust. Flame 39 (3) (1980) 219–224.
[3] H. Xu, L.A. LaPointe, Calculation of laminar flame speed and autoignition delay at high temperature and pressures, Volume 1: Large Bore Engines; Advanced Combustion; Emissions Control Systems; Instrumentation, Controls, and Hybrids, American Society of Mechanical Engineers, 2013.
[4] R. Sankaran, Propagation velocity of a deflagration front in a preheated autoigniting mixture, 9th US Natl. Combust. Meet., 2015.
[5] J. Pan, H. Wei, G. Shu, Z. Chen, P. Zhao, The role of low temperature chemistry in combustion mode development under elevated pressures, Combust. Flame 174 (2016) 179–193.
[6] A. Krisman, E.R. Hawkes, J.H. Chen, The structure and propagation of laminar flames under autoignitive conditions, Combust. Flame 188 (2018) 399–411.
[7] T. Zhang, A.J. Susa, R.K. Hanson, Y. Ju, Studies of the dynamics of autoignition assisted outwardly propagating spherical cool and double flames under shock-tube conditions, Proc. Combust. Inst. 38 (2) (2021) 2275–2283.
[8] S.D. Tse, D. Zhu, C.K. Law, Morphology and burning rates of expanding spherical flames in H2/O2/inert mixtures up to 60 atmospheres, Proc. Combust. Inst. 28 (2) (2000) 1793–1800.
[9] O. Kurata, S. Takahashi, Y. Uchiyama, Influence of preheat temperature on the laminar burning velocity of methane-air mixtures, SAE Transact. (1994) 1766–1772.
[10] Y. Wang, A. Movaghar, Z. Wang, Z. Liu, W. Sun, F.N. Egolfopoulos, Z. Chen, Laminar flame speeds of methane/air mixtures at engine conditions: performance of different kinetic models and power-law correlations, Combust. Flame 218 (2020) 101–108.
[11] M. Akram, S. Kumar, Measurement of laminar burning velocity of liquified petrolium gas air mixtures at elevated temperatures, Energy Fuels 26 (6) (2012) 3267–3274.
[12] D. Assanis, S.W. Wagnon, M.S. Wooldridge, An experimental study of flame and autoignition interactions of iso-octane and air mixtures, Combust. Flame 162 (4) (2015) 1214–1224.
[13] A.M. Ferris, A.J. Susa, D.F. Davidson, R.K. Hanson, High-temperature laminar flame speed measurements in a shock tube, Combust. Flame 205 (2019) 241–252.
[14] A.J. Susa, L. Zheng, R.K. Hanson, Schlieren-based measurements of propane flame speeds at extreme temperatures, in: 12th US National Combustion Meeting, 2021, p. 1G05.
[15] A.J. Susa, R.K. Hanson, Distortion of expanding n-heptane flames at high unburned-gas temperatures behind reflected shocks, Combust. Flame 237 (2022) 111842.
[16] A.J. Susa, R.K. Hanson, Flame image velocimetry: seedless characterization of post-reflected-shock velocities in a shock tube, Exp. Fluids (2022).
[17] A.J. Susa, L. Zheng, Z.D. Nygaard, R.K. Hanson, End-wall effects on freely propagating flames in a shock tube, in: AIAA Scitech Forum, 2022, p. 2346.
[18] A.J. Susa, High-Speed imaging studies of flames in a shock tube: refined techniques and new applications, Stanford University, 2022 Ph.D. thesis.
[19] F. Stevens, A Constant Pressure Bomb, Technical Report 176, Bureau of Standards, 1923.

Please cite this article as: A.J. Susa, L. Zheng and R.K. Hanson, Measurements of propane–O<ce:inf>2</ce:inf>–Ar laminar flame speeds at temperatures exceeding 1000 K in a shock tube, Proceedings of the Combustion Institute, https://doi.org/10.1016/j.proci.2022.07.191

[20] G.H. Markstein, Experimental and theoretical studies of flame-front stability, J. Aeronaut. Sci. 18 (3) (1951) 199–209.
[21] R. Strehlow, L. Savage, The concept of flame stretch, Combust. Flame 31 (1978) 209–211.
[22] A.P. Kelley, C.K. Law, Nonlinear effects in the extraction of laminar flame speeds from expanding spherical flames, Combust. Flame 156 (9) (2009) 1844–1851.
[23] Z. Chen, On the extraction of laminar flame speed and Markstein length from outwardly propagating spherical flames, Combust. Flame 158 (2) (2011) 291–300.
[24] X. Cai, J. Wang, H. Zhao, Y. Xie, Z. Huang, Effects of initiation radius selection and lewis number on extraction of laminar burning velocities from spherically expanding flames, Combust. Sci. Technol. 190 (2) (2018) 286–311.
[25] M.J. Hegetschweiler, J.L. Pagliaro, L. Berger, R. Hesse, J. Beeckmann, C. Bariki, H. Pitsch, G.T. Linteris, Data reduction considerations for spherical R-32 (CH2F2)-air flame experiments, Combust. Flame 237 (2022) 111806.
[26] M. Campbell, A. Tulgestke, D. Davidson, R. Hanson, A second-generation constrained reaction volume shock tube, Rev. Sci. Instrum. 85 (5) (2014) 055108.
[27] M.F. Campbell, K.G. Owen, D.F. Davidson, R.K. Hanson, Dependence of calculated postshock thermodynamic variables on vibrational equilibrium and input uncertainty, J. Thermophys. Heat Transf. 31 (3) (2017) 586–608.
[28] S. Wang, T. Parise, S.E. Johnson, D.F. Davidson, R.K. Hanson, A new diagnostic for hydrocarbon fuels using 3.41-um diode laser absorption, Combust. Flame 186 (2017) 129–139.
[29] G.S. Settles, Schlieren and Shadowgraph Techniques: Visualizing Phenomena in Transparent Media, Springer Science & Business Media, 2001, pp. 116–118.
[30] L. Zheng, A.J. Susa, R.K. Hanson, Methodology of designing compact schlieren systems using off-axis parabolic mirrors, Appl. Opt. 61 (2022) 4857–4864.
[31] M. Kass, A. Witkin, D. Terzopoulos, Snakes: active contour models, Intl. J. Comput. Vis. 1 (4) (1988) 321–331.
[32] S. van der Walt, J.L. Schönberger, J. Nunez-Iglesias, F. Boulogne, J.D. Warner, N. Yager, E. Gouillart, T. Yu, the scikit-image contributors, scikit-image: image processing in Python, PeerJ 2 (2014) e453.
[33] P. Virtanen et al, SciPy 1.0: fundamental algorithms for scientific computing in Python, Nat. Methods 17 (2020) 261–272.
[34] M. Spivak, A Comprehensive Introduction to Differential Geometry, Vol. 5, Publish or Perish, Incorporated, 1975.
[35] A. Savitzky, M.J. Golay, Smoothing and differentiation of data by simplified least squares procedures, Anal. Chem. 36 (8) (1964) 1627–1639.
[36] M.P. Burke, Z. Chen, Y. Ju, F.L. Dryer, Effect of cylindrical confinement on the determination of laminar flame speeds using outwardly propagating flames, Combust. Flame 156 (4) (2009) 771–779.
[37] D.G. Goodwin, R.L. Speth, H.K. Moffat, B.W. Weber, Cantera: an object-oriented software toolkit for chemical kinetics, thermodynamics, and transport processes, 2021. Version 2.5.1.
[38] C.W. Zhou, et al., An experimental and chemical kinetic modeling study of 1, 3-butadiene combustion: ignition delay time and laminar flame speed measurements, Combust. Flame 197 (2018) 423–438.
[39] Student, The probable error of a mean, Biometrika 6 (1) (1908) 1–25.
[40] Q.-D. Wang, S. Panigrahy, S. Yang, S. Martinez, J. Liang, H.J. Curran, Development of multipurpose skeletal core combustion chemical kinetic mechanisms, Energy Fuels 35 (8) (2021) 6921–6927.
[41] U. of California at San Diego, Chemical-kinetic mechanisms for combustion applications, 2016.
[42] A.A. Konnov, A. Mohammad, V.R. Kishore, N.I. Kim, C. Prathap, S. Kumar, A comprehensive review of measurements and data analysis of laminar burning velocities for various fuel+air mixtures, Prog. Energy Combust. 68 (2018) 197–267.
[43] J. Huo, S. Yang, Z. Ren, D. Zhu, C.K. Law, Uncertainty reduction in laminar flame speed extrapolation for expanding spherical flames, Combust. Flame 189 (2018) 155–162.
[44] A.J. Susa, A.M. Ferris, D.F. Davidson, R.K. Hanson, Experimental measurement of laminar burning velocity of n-heptane at variable extents of reactions in a shock tube, Int. Symp. on Shock Waves 32, 2019.
[45] W. Liu, Y. Qi, R. Zhang, Z. Wang, Flame propagation and auto-ignition behavior of iso-octane across the negative temperature coefficient (NTC) region on a rapid compression machine, Combust. Flame 235 (2022) 111688.

Please cite this article as: A.J. Susa, L. Zheng and R.K. Hanson, Measurements of propane–O<ce:inf>2</ce:inf>–Ar laminar flame speeds at temperatures exceeding 1000 K in a shock tube, Proceedings of the Combustion Institute, https://doi.org/10.1016/j.proci.2022.07.191